Orbital-adapted electronic structure and anisotropic transport in γ-Al_2O_3/$SrTiO_3$ heterostructure

Xiaoping Yang [1], Haibin Su [2,*] and Gang Wu [3,†]

[1] *Anhui Province Key Laboratory of Condensed Matter Physics at Extreme Conditions, High Magnetic Field Laboratory, Chinese Academy of Sciences, Hefei 230031, China*

[2] *Department of Chemistry, The Hong Kong University of Science and Technology, Hong Kong 999077, China*

[3] *Institute of High Performance Computing, 1 Fusionopolis Way, 16-16 Connexis, Singapore 138632, Singapore*

(Received 28 August 2019; revised manuscript received 17 November 2019; published 13 January 2020)

High electron mobility is pivotal in engineering oxide interfaces for electronic devices. Here, interfacial structure and physical behaviors of γ-Al_2O_3/$SrTiO_3$ spinel/perovskite heterostructure are explored to understand the microscopic origin of its extremely high electron mobility (1.4×10^5 cm^2 V^{-1} s^{-1} at 2 K). Lattice mismatch at interface and intrinsic Al cation vacancies result in unexpected interfacial reconstruction and anisotropic electronic behavior. The spontaneous polarization in the γ-Al_2O_3 part leads to an insulator-metal transition observed experimentally, even if the thickness of γ-Al_2O_3 is only one unit cell, and a strong internal electric field can be as large as 142 mV/Å, roughly 1.8 times the experimentally observed value of 80.1 mV/Å in $LaAlO_3$/$SrTiO_3$. As a result, unlike only in-plane slightly occupied Ti-d_{xy} subbands in the conventional $SrTiO_3$-based perovskite/perovskite heterostructure, all three t_{2g} orbitals have charge exchange with the surfacial O-2p orbitals in γ-Al_2O_3/$SrTiO_3$; especially, the preferential orbital occupation is out-of-plane Ti-d_{xz}/Ti-d_{yz} at the interface. Nontrivial orbital occupation and complicated interfacial reconstruction result in large group velocity and a high density of states at the Fermi level and therefore serve as the origins of extremely high electron mobility and high carrier concentration. The physical mechanism revealed in our work offers insight into the creation of high-mobility nanoscale electronic devices.

DOI: 10.1103/PhysRevMaterials.4.016001

I. INTRODUCTION

As early as 100 years ago, researchers like Donnan had realized the potential to take advantage of the "two-dimensional" phase at surfaces or interfaces that separate different sorts of matters in bulk [1]. The fast development of the experimental interface technology in the past decades has motivated the research effort to study and design the extraordinary physical properties of transitional metal materials with interfaces. Here the interface can be used to modulate the electronic structure around the Fermi level for manipulating physical properties and generating phenomena which are absent in the bulk constituents, due to the rearrangement of orbitals, charge, spins, and lattice and the resulting rebalancing of their mutual interactions [2–6]. These emergent phases, such as high mobility, superconductivity, tunable spin-orbit coupling, multiferroelectricity, and magnetism, etc., hold promising potential for tailor-made functionalities useful in, e.g., microelectronics, data storage, and sensor technology.

Typically, owing to the rapid progress in atomic-scale control of complex oxide heterostructure (HS) growth, a two-dimensional electron gas (2DEG) has been observed at the (001)-oriented heterointerface between two band-gap insulators of perovskite $LaAlO_3$ (LAO) and $SrTiO_3$ (STO) [7–13]. More recently, a 2DEG with extremely high carrier mobilities, exceeding 10^5 cm^2 V^{-1} s^{-1} at 2 K, is fabricated at a (001)-oriented epitaxial spinel/perovskite interface between γ-alumina (γ-Al_2O_3, GAO) and STO [14–21]. The interface conduction depends strongly on GAO film thickness and also sample temperature. At 700°C, the critical thickness for an insulator-metal transition can be as low as one unit cell [15]. In addition, 2DEG found at the interface of GAO/STO displays anisotropic electronic transport [22,23]. The origin of the emergent unusual quantum states and transport phenomenon is currently under debate. Some studies attribute them to the altered crystal field at the interface and symmetry breaking of the interfacial structural units, but the exact nature of interfacial structural change and its effect on physical properties are unclear up to now.

Herein, in order to solve this conundrum, we conduct a detailed investigation and analysis of the interfacial structural strain, electronic properties, and Ti-t_{2g} orbital physics of spinel/perovskite HS GAO/STO. HS is found to carry out interfacial reconstruction to a lower energy configuration due to the intrinsic Al cation vacancies and lattice mismatch at the interface. Associated with this interfacial transition, electronic behavior presents strong anisotropy observed experimentally. Strong spontaneous polarized potential across the GAO part induces out-of-plane electronic reconstruction; however, the extra electrons from surfacial oxygens occupy the three Ti-t_{2g} states rather than only the Ti-d_{xy} state in the LAO/STO case, inducing larger group velocity and higher carrier density at the Fermi level. Very interestingly, the preferential orbital occupation is out-of-plane Ti-d_{xz}/Ti-d_{yz} in the STO-1 layer at the interface, consistent with the result of resonant soft x-ray linear dichroism [21].

*Corresponding author: haibinsu@ust.hk

†Corresponding author: wug@ihpc.a-star.edu.sg

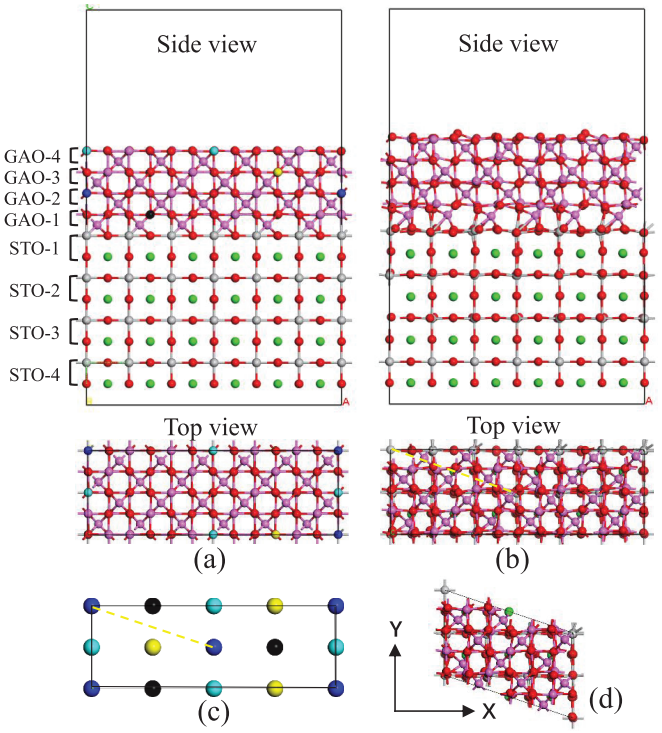

FIG. 1. Schematic geometrical structures of GAO/STO HS (a) before and (b) after atomic optimization. (c) The locations (top view) of intrinsic Al cation vacancies at octahedral sites in different GAO layers are labeled by different colors, and the same color mark is used in panel (a). (d) Optimized HS in its pseudohexagonal primitive cell due to interfacial reconstruction in the xy plane.

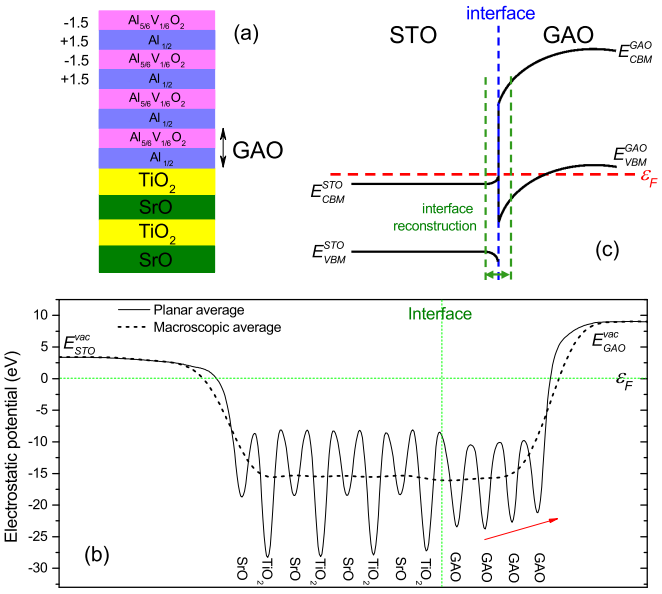

FIG. 2. (a) A sketch of the GAO/STO heterostructure. (b) Macroscopic average and planar average of the electrostatic potential. (c) Schematic band diagram of the GAO/STO heterostructure.

II. RESULTS AND DISCUSSION

Usually, the crystal structure of γ-Al_2O_3 is described as a spinel AB_2O_4 with Al cation vacancies at A or B sites. Its fcc cubic cell has a spinel unit $4[A_2\text{-}B_4O_8]$ with the lattice constant of $a = 7.911$ Å [24], containing 56 atoms: 8 Al atoms in tetrahedral A sites, 16 Al in octahedral B sites, and 32 O in a fcc array. Appropriate cation vacancies must be introduced to satisfy the Al_2O_3 stoichiometry. Theoretically, first-principles calculations indicate that the cation vacancies prefer octahedral positions, and they tend to distribute far away from each other [25]. Therefore, in our first-principles investigation of γ-$Al_2O_3/SrTiO_3$ heterostructure, we focus on the case of octahedral vacancy occupied.

In order to minimize the lattice mismatch between γ-Al_2O_3 and $SrTiO_3$, a two-dimensional (2D) supercell was constructed in Fig. 1(a). We took the sextuple and duplation of lattice constant of bulk $SrTiO_3$ (23.43 and 7.81 Å) as the in-plane lattice constant a and b of the γ-$Al_2O_3/SrTiO_3$ heterostructure, respectively. An eight-cation vacancy on octahedral sites was decided according to the interaction minimization between vacancies, as shown in Fig. 1(c). For simulating substrate effect, we relaxed atomic internal coordinates except for those in the lowest STO-4 layer.

The optimized heterostructure and its pseudohexagonal primitive cell are shown in Figs. 1(b) and 1(d), respectively. Compared to the LAO/STO HS, the structure properties and the polarization distortion are obviously more complicated in the GAO/STO HS. An atomic interfacial reconstruction occurs, due to interfacial symmetry breaking, Al cation vacancy, and big structure differences between spinel and perovskite, and finally the HS reaches a lower energy configuration in the pseudohexagonal phase [Fig. 1(d)]. Structural distortion in the GAO-1 layer at the interface is much larger than that in other GAO layers, which finally affects the electrostatic potential and electronic properties discussed below. The local ionic dipole moment [see Fig. 2(a)] in the HS induces inevitably an internal polarized electric field across γ-Al_2O_3 and leads to increased Ti-O bond lengths along the z direction. In order to illustrate the effect of the polarized field on the energy gap, we show the planar averaged (PA) electrostatic potential [26] and its macroscopic average (MA) along the z direction perpendicular to the interface of heterostructure in Fig. 2(b). In the γ-Al_2O_3 region, the electrostatic potential increases gradually and eventually makes the valence band edge of the surface layer cross over the Fermi level, as can be seen from Fig. 3. The valence band shift (VBS) in the γ-Al_2O_3 region can be obtained simply as the difference between the valence band edges of the surface and interface layers, i.e., $E_{\mathrm{VBS}}^{\mathrm{GAO}} = E_{\mathrm{V}}^{\mathrm{GAO-4}} - E_{\mathrm{V}}^{\mathrm{GAO-1}}$, from which the internal electric field is estimated to be 142 mV/Å, roughly 1.8 times the experimentally observed value of 80.1 mV/Å in the LAO/STO HS [27], potentially leading to larger carrier concentration at the interface. It is worth noting that the MA potential presents a smooth evolution at the interface, absolutely different from the abrupt change in the LAO/STO HS, due to interfacial reconstruction and intrinsic Al cation vacancies.

The layer-projected densities of states are shown in Fig. 3. The polarized GAO produces a potential increment beyond the band gap of STO, brings three Ti-t_{2g} states of STO and the O-p_x, p_y states of the GAO surface across the Fermi level, and drives an insulator-metal transition in the HS. The electric field discontinuity in the GAO part leads to the upshifting of

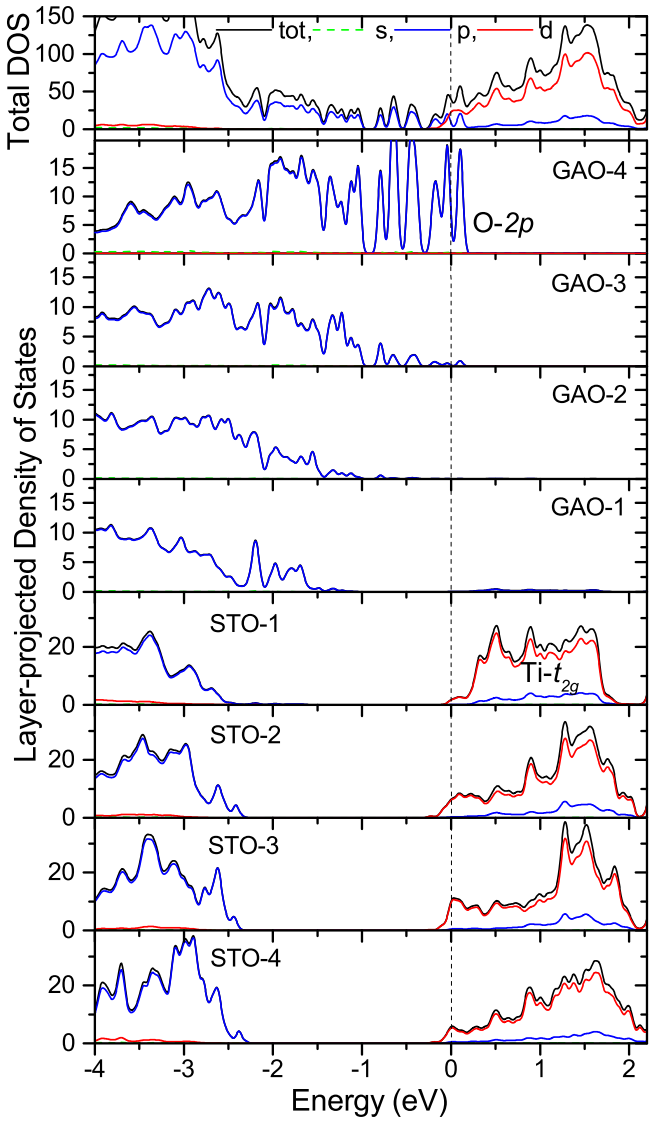

FIG. 3. Layer-projected density of states of the GAO/STO heterostructure after interfacial reconstruction.

the valence band edge, and positive and negative monopole charges accumulate at the GAO surface and on the STO side, respectively, in the metallic phase, which is confirmed by the partial charge density in Fig. 5.

The distinct formation mechanism of a 2DEG in GAO/STO is displayed in the schematic band diagram in Fig. 2(c). Interface reconstruction results in the strained local structure and hence the changed local electronic structure. Meanwhile, out-of-plane electronic reconstruction comprises the formation of both holes at the surface and electrons at the interface. This stands for the forming of a Schottky barrier.

In Fig. 4(a), we show the Ti-O and Al-O polyhedral structures in the optimized GAO/STO HS. The TiO_6 octahedral structural feature remains intact at the interface, with the top apical oxygens coming from the GAO-1 layer. Figure 4(c) shows the band dispersion of the GAO/STO heterostructure in a 1-eV region around the Fermi level $\varepsilon_F \equiv 0$ and along the symmetry lines K-Γ-M-K′-N-Γ-K′ = (0.556, 0.278, 0)-(0, 0, 0)-(0.5, 0, 0)-(0.444, −0.278, 0)-(0, −0.5, 0)-(0, 0, 0)-(0.444, −0.278, 0), from which we can conclude that the electronic properties of HS around ε_F are mainly controlled by the Ti-3d and O-2p orbitals. Due to the asymmetry geometry and quantum confinement, the degeneracy of the original bulk Ti-3d bands is broken and band splitting occurs in the HS. We plot the Ti-t_{2g} fat band of four STO layers in different colors to disclose their orbital contribution. One can find that the Ti-t_{2g} band edge shifts below the Fermi level and overlaps with some flat bands with very small energy dispersion.

In order to better understand the physics origin of the insulator-metal transition, we plot the partial charge density of the valence bands from −0.25 eV to the Fermi level in Fig. 5. The Ti-t_{2g} bands are found to exchange holes with the electrons of the O-2p bands. Obviously, the flat bands around ε_F are contributed by O-2p bands, and insulator-metal transition originates from charge transfer between Ti-t_{2g} orbitals and O-2p at GAO surface, consistent with the features in the band structures in Fig. 4(c). The partial occupied Ti-t_{2g} states do not locate at the STO-1 interface only but also spread into the whole STO part. Therefore these partial occupied states actually can be regarded as the linear combinations of Ti-t_{2g} from different TiO_2 planes.

Based on our experience from LAO/STO simulation [11], the thickness of the polar layer determines the amount of charge transfer to Ti-3d orbitals, despite that the exact distribution of the induced Ti-3d electrons in STO is dependent on the simulation model. Nevertheless, in both the heterostructure model with vacuum or the superlattice model [28,29], Ti-3d states always spread into all STO layers. By simulating a LAO/STO superlattice with 23 layers of STO [29], the authors observed the attenuation of the charge density away from the interface, and they observed that the 2DEG is confined in STO within about 1 nm from the interface and the rest of the occupied Ti-3d states in the region >1 nm can be explained by quantum tunneling. It should be pointed out that the Ti-d_{xy} subband always has lower energy in both the interface STO layer and the noninterface STO layer, regardless of the thickness of STO. This is determined by the less distorted TiO_6 octahedral at the interface of the LAO/STO HS or superlattice.

In Figs. 4(c) and 4(d), extra electrons from surfacial oxygens occupy the three Ti-t_{2g} states in the GAO/STO HS rather than only the Ti-d_{xy} state in the LAO/STO case. Since the lowest three bands crossing the Fermi level are parabolic-like and occupied by Ti-d_{xy} states around the Γ point, we draw the reference Fermi level ε_F^{LAO} (red dashed and solid lines) of the LAO/STO case in Figs. 4(c) and 4(d). Obviously, the occupation of out-of-plane Ti-d_{xz} and Ti-d_{yz} states in the GAO/STO HS leads to the relative elevation of the Fermi level and hence the larger slopes of the Ti-d bands at the Fermi level, and in the meantime more bands cross the Fermi level, which further induces larger group velocity and higher carrier density at the Fermi level. On the other hand, due to the hybridization with Ti-d_{xz}/Ti-d_{yz} orbitals and the anti-crossing effect, the effective masses of some Ti-d_{xy} orbitals decrease considerably and this implies higher mobility (for more details, please see Supplemental Material [30]). Ti-d_{xy} subbands are lower than the Ti-d_{xz}/Ti-d_{yz} subbands at the noninterfacial

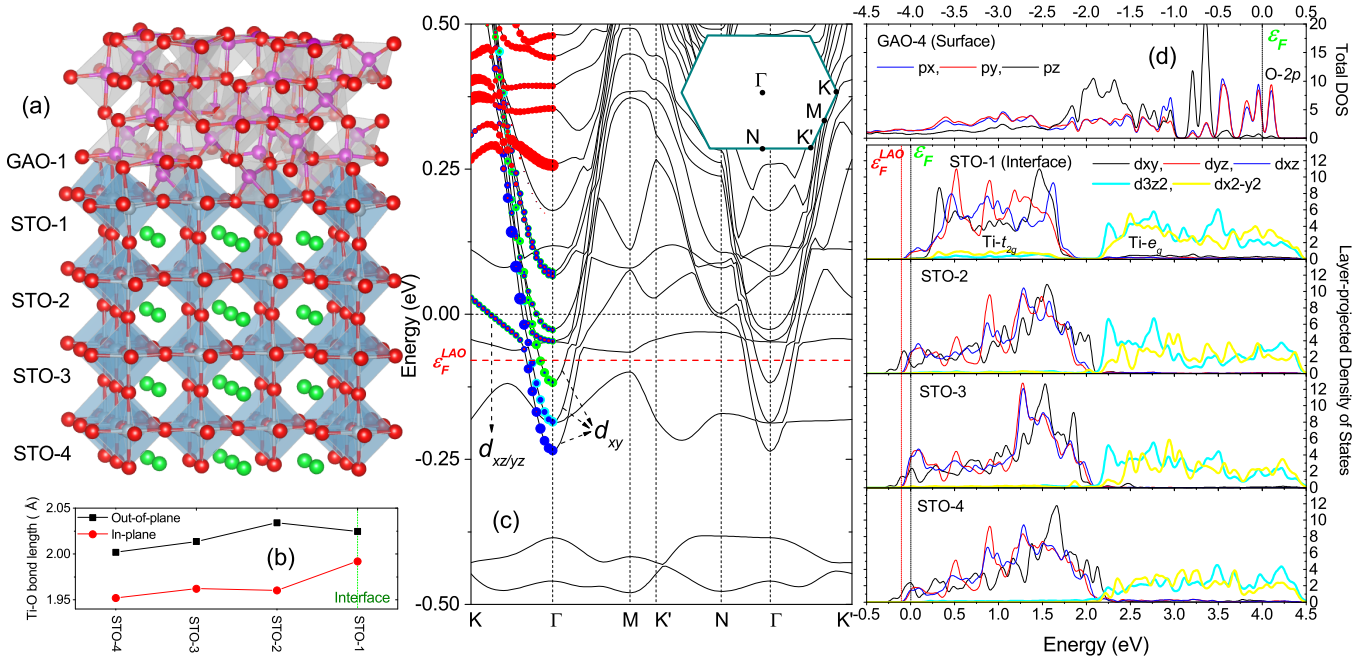

FIG. 4. (a) Schematic diagram of Ti-O and Al-O polyhedral structures in the optimized GAO/STO HS. (b) In-plane and out-of-plane Ti-O bond length in the different STO layers. (c) generalized gradient approximation (GGA) band structures of the GAO/STO heterostructure. The Fermi level ε_F is set at zero. The Ti-t_{2g} orbital contributions in four different STO layers are disclosed by fat bands along K-Γ in cyan (STO-4), green (STO-3), blue (STO-2), and red (STO-1), respectively. The inset is the first Brillouin zone of the HS in the pseudohexagonal phase. (d) Layer-projected density of states of Ti-t_{2g} orbitals and surfacial O-2p orbitals. The reference Fermi level ε_F^{LAO} of the LAO/STO case is shown by the horizontal red dashed line in panel (c) and the red solid line in panel (d).

layer due to the larger in-plane hopping integrals. Interestingly, the t_{2g} band width becomes smaller and the Ti-d_{xy} state becomes unoccupied at the STO-1 interface, resulting from the larger in-plane Ti-O bond length and the smaller difference between in-plane and out-of-plane bond lengths [see Fig. 4(b)]. The peak intensities of d_{xy} and d_{xz}/d_{yz} projected density of states around the Fermi level present nonsystematic variation behaviors with the layer numbers, probably due to the simultaneous effects of the internal electric field and the strain field. Finite-size effect and the existence of an open surface to the vacuum may also contribute to the nonsystematic trend. Therefore, in our study of spine/perovskite GAO/STO HSs, we focus mainly on the qualitative overturn of the Ti-t_{2g} orbital occupation in the STO-1 interface layer against that in the noninterface layer, originating from serious structure mismatch at interface.

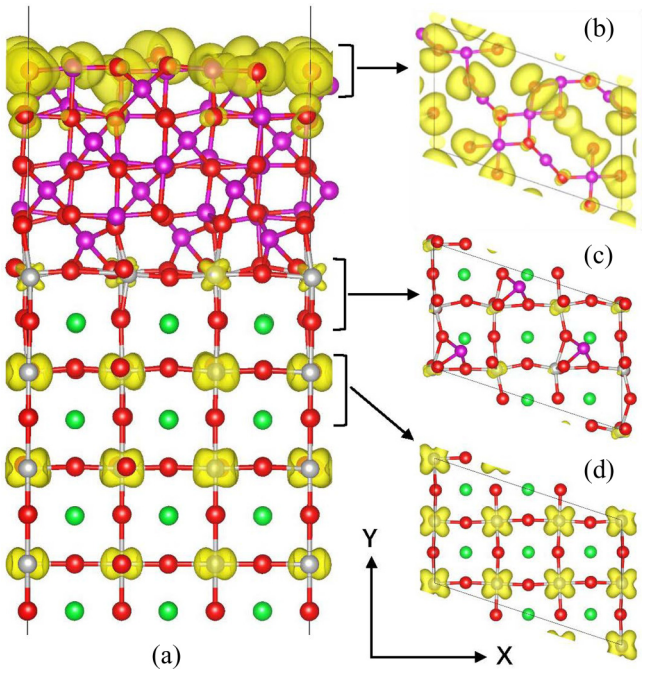

FIG. 5. Partial charge density isosurfaces for the valence bands from −0.25 eV to the Fermi level. (a) Side view of the whole HS. Top views of (b) the surfacial GAO-4 layer, (c) the interfacial STO-1 layer, and (d) the noninterfacial STO-2 layer.

In all archetypical reported (001)-oriented STO-based perovskite/perovskite HSs including the LAO/STO HS mentioned above, the preferential occupation of the two-dimensional electron gases is the in-plane Ti-d_{xy} state [35–41]. In sharp contrast to this, the investigated electronic structure of the spinel/perovskite HS GAO/STO demonstrates that the preferential occupation is the out-of-plane Ti-d_{xz}/Ti-d_{yz} states for interfacial electrons in the STO-1 layer, which is consistent with the result of resonant soft x-ray linear dichroism [21,42]. It can be anticipated that the wave-function character of Ti-d_{xz}/Ti-d_{yz} is enhanced further in interfacial TiO_2 planes with the increased layer number of GAO. However, in noninterfacial STO-2, -3, and -4 layers, the Ti-d_{xy} subband is lower than the Ti-d_{xz}/Ti-d_{yz} subbands in STO-1, which is different from experimental observation. There are two possible causes for this discrepancy: (i) The main feature of x-ray absorption signal may correspond to the density of states at the Fermi level of 3d states, not the

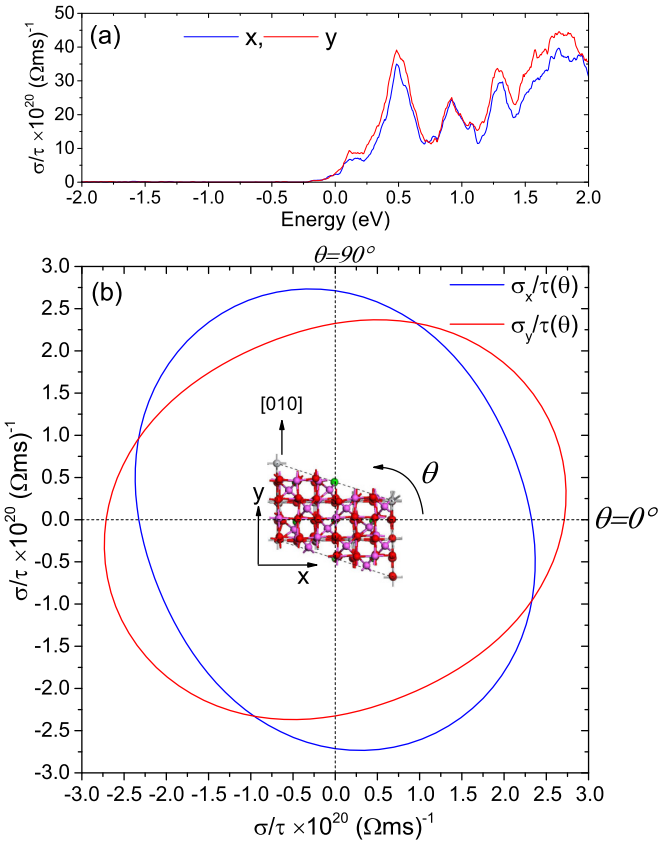

FIG. 6. Anisotropic electrical conductivity (a) and polar plot of the angular dependence of anisotropic electrical conductivity (b) at 2 K in the *xy* plane of the HS.

lowest available states that are well below the Fermi level in the present case. (ii) When the STO is even thicker, the band edge of Ti-d_{xy} subband shifts higher, and the 3*d* electrons may distribute mainly in the Ti-d_{xz}/Ti-d_{yz} subbands.

In Ref. [42], Cao *et al.* explain the observed out-of-plane orbital occupation by the altered crystal field (with the missing upper apical O atoms) in the STO-1 layer at the interface. However, in our work, we find that the octahedral crystal field splitting between t_{2g} and e_g still holds at the interfacial STO-1 layer, even bigger than that in other STO layers. Therefore, the cause of the partial occupied out of plane Ti-d_{xz}/Ti-d_{yz} states in the STO-1 layer is not the proposed altered-crystal field at the interface [42], but rather a complex interfacial chemical environment, e.g., tetrahedral Al cation, octahedral Al cation vacancies, lattice mismatch, and unexpected interface reconstruction. Significantly, symmetry breaking and complex interface reconstruction result in orbital splitting between Ti-d_{xz} and Ti-d_{yz} at the interface, and also between O-p_x and O-p_y at the surface of the HS, which finally induces large anisotropic electrical conductivity σ/τ in the *xy* plane of the HS in Fig. 6(a). Furthermore, σ/τ is simulated with rotating the in-plane electric field. The angle θ between the electric field and the [100] direction was varied from 0° to 360°. The angular dependence of intrinsic σ/τ at 2 K is shown in Fig. 6(b), which reveals the obvious anisotropic character. The ratio $\sigma_{\max}/\sigma_{\min}$ is 1.26, which is consistent with the experimental result of 1.33 for sample I in Ref. [22].

III. CONCLUSIONS

In summary, we have find unusual interfacial reconstruction, nontrivial orbital physics, and anisotropic electronic properties in spinel/perovskite GAO/STO HSs, which are much different than those in STO-based perovskite/perovskite LAO/STO HSs. Strong polarized internal electric fields and interfacial reconstruction play critical roles in the determination of orbital physics in spinel/perovskite GAO/STO HSs, which are the origin of higher carrier density at the Fermi level, higher electron mobility, and abnormal interface transport observed experimentally. Our studies indicate that GAO/STO HSs are promising candidates for nanoscale oxide electronic devices and technology, e.g., metal-semiconductor junctions in Schottky diodes and even 2D oxide-metal hybrid devices with extraordinary magnetoresistance. Also, the intrinsic physical mechanism revealed in our study offers insight into the creation of new high-mobility nanoscale electronic devices.

IV. THEORETICAL METHODS AND MODELS

The numerical density functional calculations were based on the plane-wave basis and projector augmented-wave method [43,44] as implemented in the Vienna *Ab initio* Simulation Package [45–48]. A Perdew-Burke-Ernzerhof exchange-correlation functional [49,50] within the framework of the generalized gradient approximation was adopted, with a uniform plane-wave cutoff energy of 520 eV for the calculations of electronic band structures. For the heterostructure model, periodic boundary conditions were assumed along all the directions, and a thick vacuum layer was introduced around the slab to prohibit the out-of-plane electronic and dipole-dipole interactions between neighboring images of the heterostructures. The Monkhorst-Pack method was employed to generate the *k*-mesh, and the *k*-point spacing was limited to 0.02 Å^{-1}. The heterostructures were fully optimized by employing the conjugate gradient technique, and no force on the atoms exceeded 0.01 eV/Å in the final geometry.

Within the commonly adopted constant relaxation time approximation (CRTA), the electrical conductivity can be expressed as

$$\sigma(T,\mu) = -\frac{\tau}{\Omega}\int dE \frac{\partial f}{\partial E}\mathcal{T}(E),$$

where the relaxation time τ is assumed to be a constant along different directions, Ω is the volume of the simulation cell, and $f = f_{\mu,T}(E)$ denotes the Fermi distribution function, which is a function of energy E. The transmission $\mathcal{T}(E)$ can be written as

$$\mathcal{T}(E) = \frac{e^2}{N}\sum_{i,\vec{k}} \delta(E - \varepsilon_{i,\vec{k},\sigma})\vec{v}_{\vec{k}}\vec{v}_{\vec{k}}.$$

Here $\vec{v}_{\vec{k}} = (1/\hbar)\nabla_{\vec{k}}\varepsilon_{i,\vec{k}}$ is the group velocity of the charge carrier in *i*th band. Because we focus on a narrow energy window (around the transmission peak near the Fermi level), we consider the CRTA to be well justified. The energy dispersion $\varepsilon_{i,\vec{k}}$ and the group velocity were taken from the first-principles band structure calculations with dense $\vec{k}$-point mesh, and then BOLTZTRAP code [51] was used to calculate σ/τ.

ACKNOWLEDGMENTS

This work was supported by the National Key Research and Development Program of China (Grants No. 2018YFA0305700 and No. 2017YFA0403600), the National Natural Science Foundation of China (NSFC) (Grants No. 11674325 and No. U1632162). A portion of this work was supported by the High Magnetic Field Laboratory of Anhui Province. The work was also supported in part by the Society of Interdisciplinary Research (SOIRÉE).

[1] F. G. Donnan, Nature (London) **112**, 867 (1923).
[2] J. Mannhart and D. G. Schlom, Science **327**, 1607 (2010).
[3] H. Y. Hwang, Y. Iwasa, M. Kawasaki, B. Keimer, N. Nagaosa, and Y. Tokura, Nat. Mater. **11**, 103 (2012).
[4] J. A. Sulpizio, S. Ilani, P. Irvin, and J. Levy, Annu. Rev. Mater. Res. **44**, 117 (2014).
[5] J. Chakhalian, J. W. Freeland, A. J. Millis, C. Panagopoulos, and J. M. Rondinelli, Rev. Mod. Phys. **86**, 1189 (2014).
[6] F. Hellman, A. Hoffmann, Y. Tserkovnyak, G. S. D. Beach, E. E. Fullerton, C. Leighton, A. H. MacDonald, D. C. Ralph, D. A. Arena, H. A. Dürr *et al.*, Rev. Mod. Phys. **89**, 025006 (2017).
[7] A. Ohtomo and H. Y. Hwang, Nature (London) **427**, 423 (2004).
[8] S. Thiel, G. Hammerl, A. Schmehl, C. Schneider, and J. Mannhart, Science **313**, 1942 (2006).
[9] A. Brinkman, M. Huijben, M. van Zalk, J. Huijben, U. Zeitler, J. C. Maan, W. G. van der Wiel, G. Rijnders, D. H. A. Blank, and H. Hilgenkamp, Nat. Mater. **6**, 493 (2007).
[10] E. Benckiser, M. W. Haverkort, S. Brück, E. Goering, S. Macke, A. Frañó, X. Yang, O. K. Andersen, G. Cristiani, H. U. Habermeier, A. V. Boris, I. Zegkinoglou, H. J. Kim, V. Hinkov, and B. Keimer, Nat. Mater. **10**, 189 (2011).
[11] X. Yang and H. Su, ACS Appl. Mater. Interfaces **3(10)**, 3819 (2011).
[12] J.-S. Lee, Y. W. Xie, H. K. Sato, C. Bell, Y. Hikita, H. Y. Hwang, and C.-C. Kao, Nat. Mater. **12**, 703 (2013).
[13] N. Reyren, S. Thiel, A. D. Caviglia, L. Fitting Kourkoutis, G. Hammerl, C. Richter, C. W. Schneider, T. Kopp, A.-S. Rüetschi, D. Jaccard, M. Gabay, D. A. Muller, J.-M. Triscone, and J. Mannhart, Science **317**, 1196 (2007).
[14] Y. Z. Chen, N. Bovet, F. Trier, D. V. Christensen, F. M. Qu, N. H. Andersen, T. Kasama, W. Zhang, R. Giraud, J. Dufouleur, T. S. Jespersen, J. R. Sun, A. Smith, J. Nygard, L. Lu, B. Büchner, B. G. Shen, S. Linderoth, and N. Pryds, Nat. Commun. **4**, 1371 (2013).
[15] Y. Z. Chen, N. Bovet, T. Kasama, W. W. Gao, S. Yazdi, C. Ma, N. Pryds, and S. Linderoth, Adv. Mater. **26**, 1462 (2014).
[16] K. J. Kormondy, A. B. Posadas, T. Q. Ngo, S. Lu, N. Goble, J. Jordan-Sweet, X. P. A. Gao, D. J. Smith, M. R. McCartney, J. G. Ekerdt, and A. A. Demkov, J. Appl. Phys. **117**, 095303 (2015).
[17] P. Schütz, F. Pfaff, P. Scheiderer, Y. Z. Chen, N. Pryds, M. Gorgoi, M. Sing, and R. Claessen, Phys. Rev. B **91**, 165118 (2015).
[18] T. Q. Ngo, N. J. Goble, A. Posadas, K. J. Kormondy, S. Lu, M. D. McDaniel, J. Jordan-Sweet, D. J. Smith, X. P. A. Gao, A. A. Demkov, and J. G. Ekerdt, J. Appl. Phys. **118**, 115303 (2015).
[19] S. Lu, K. J. Kormondy, T. Q. Ngo, T. Aoki, A. Posadas, J. G. Ekerdt, A. A. Demkov, M. R. McCartney, and D. J. Smith, Appl. Phys. Lett. **108**, 051606 (2016).
[20] D. V. Christensen, Y. Frenkel, P. Schütz, F. Trier, S. Wissberg, R. Claessen, B. Kalisky, A. Smith, Y. Z. Chen, and N. Pryds, Phys. Rev. Appl. **9**, 054004 (2018).
[21] J. R. L. Mardegan, D. V. Christensen, Y. Z. Chen, S. Parchenko, S. R. V. Avula, N. Ortiz-Hernandez, M. Decker, C. Piamonteze, N. Pryds, and U. Staub, Phys. Rev. B **99**, 134423 (2019).
[22] K. Wolff, R. Schäfer, M. Meffert, D. Gerthsen, R. Schneider, and D. Fuchs, Phys. Rev. B **95**, 245132 (2017).
[23] D. Fuchs, K. Wolff, R. Schäfer, R. Thelen, M. Le Tacon, and R. Schneider, AIP Adv. **7**, 056410 (2017)
[24] R. S. Zhou and R. L. Snyder, Acta Crystallogr., Sect. B **47**, 617 (1991).
[25] G. Gutiérrez, A. Taga, and B. Johansson, Phys. Rev. B **65**, 012101 (2001).
[26] A. Baldereschi, S. Baroni, and R. Resta, Phys. Rev. Lett. **61**, 734 (1988).
[27] G. Singh-Bhalla, C. Bell, J. Ravichandran, W. Siemons, Y. Hikita, S. Salahuddin, A. F. Hebard, H. Y. Hwang, and R. Ramesh, Nat. Phys. **7**, 80 (2011).
[28] Z. S. Popovic, S. Satpathy, and R. M. Martin, Phys. Rev. Lett. **101**, 256801 (2008).
[29] K. Janicka, J. P. Velev, and E. Y. Tsymbal, Phys. Rev. Lett. **102**, 106803 (2009).
[30] See Supplemental Material at http://link.aps.org/supplemental/10.1103/PhysRevMaterials.4.016001 for detailed information on the effective mass calculations of the three Ti-d_{xy} bands at the crossing points with the Fermi level, which includes Refs. [31–34].
[31] Z. Zhong, A. Tóth, and K. Held, Phys. Rev. B **87**, 161102(R) (2013).
[32] H.-L. Hu, A. Pham, R. Tilley, R. Zeng, T. T. Tan, C.-H. (Charlie) Kong, R. Webster, D. Wang, and S. Li, ACS Appl. Mater. Interfaces **10**, 20950 (2018).
[33] A. H. Reshak, RSC Adv. **6**, 92887 (2016).
[34] A. Janotti, D. Steiauf, and C. G. Van de Walle, Phys. Rev. B **84**, 201304(R) (2011).
[35] Y. Cao, Z. Yang, M. Kareev, X. Liu, D. Meyers, S. Middey, D. Choudhury, P. Shafer, J. Guo, J. W. Freeland, E. Arenholz, L. Gu, and J. Chakhalian, Phys. Rev. Lett. **116**, 076802 (2016).
[36] M. Salluzzo, J. C. Cezar, N. B. Brookes, V. Bisogni, G. M. De Luca, C. Richter, S. Thiel, J. Mannhart, M. Huijben, A. Brinkman, G. Rijnders, and G. Ghiringhelli, Phys. Rev. Lett. **102**, 166804 (2009).
[37] M. Salluzzo, S. Gariglio, X. Torrelles, Z. Ristic, R. Di Capua, J. Drnec, M. Moretti Sala, G. Ghiringhelli, R. Felici, and N. B. Brookes, Adv. Mater. **25**, 2333 (2013).
[38] M. Salluzzo, S. Gariglio, D. Stornaiuolo, V. Sessi, S. Rusponi, C. Piamonteze, G. M. De Luca, M. Minola, D. Marré, A. Gadaleta, H. Brune, F. Nolting, N. B. Brookes, and G. Ghiringhelli, Phys. Rev. Lett. **111**, 087204 (2013).
[39] D. Pesquera, M. Scigaj, P. Gargiani, A. Barla, J. Herrero-Martín, E. Pellegrin, S. M. Valvidares, J. Gázquez, M. Varela,

N. Dix, J. Fontcuberta, F. Sánchez, and G. Herranz, Phys. Rev. Lett. **113**, 156802 (2014).
[40] G. Herranz, G. Singh, N. Bergeal, A. Jouan, J. Lesueur, J. Gázquez, M. Varela, M. Scigaj, N. Dix, F. Sánchez, and J. Fontcuberta, Nat. Commun. **6**, 6028 (2015).
[41] Y. J. Chang, L. Moreschini, A. Bostwick, G. A. Gaines, Y. Su Kim, A. L. Walter, B. Freelon, A. Tebano, K. Horn, and E. Rotenberg, Phys. Rev. Lett. **111**, 126401 (2013).
[42] Y. Cao, X. Liu, P. Shafer, S. Middey, D. Meyers, M. Kareev, Z. Zhong, J.-W. Kim, P. J. Ryan, E. Arenholz, and J. Chakhalian, npj Quantum Mater. **1**, 16009 (2016).
[43] G. Kresse and D. Joubert, Phys. Rev. B **59**, 1758 (1999).
[44] P. E. Blöchl, Phys. Rev. B **50**, 17953 (1994).
[45] G. Kresse and J. Hafner, Phys. Rev. B **47**, 558 (1993).
[46] G. Kresse and J. Hafner, Phys. Rev. B **49**, 14251 (1994).
[47] G. Kresse and J. Furthmüller, Phys. Rev. B **54**, 11169 (1996).
[48] G. Kresse and J. Furthmüller, Comput. Mater. Sci. **6**, 15 (1996).
[49] D. M. Ceperley and B. J. Alder, Phys. Rev. Lett. **45**, 566 (1980).
[50] J. P. Perdew, K. Burke, and M. Ernzerhof, Phys. Rev. Lett. **77**, 3865 (1996).
[51] G. K. H. Madsen and D. J. Singh, Comput. Phys. Commun. **175**, 67 (2006).